Nuclear Inst. and Methods in Physics Research, A 985 (2021) 164704

Contents lists available at ScienceDirect

Nuclear Inst. and Methods in Physics Research, A

journal homepage: www.elsevier.com/locate/nima

Comparison of heuristic and deterministic algorithms in neutron coded imaging reconstruction

Mingfei Yan [a], Huasi Hu [a,*], Guang Hu [a], Zhihua Liu [b], Chao He [c], Qiang Yi [c]

[a] School of Energy and Power Engineering, Xi'an Jiaotong University, Xi'an 710049, China
[b] Department of Nuclear, Plasma and Radiological Engineering, University of Illinois at Urbana-Champaign, Champaign 61820, USA
[c] Institute of Nuclear Physics and Chemistry, China Academy of Engineering Physics, Mianyang 621900, China

ARTICLE INFO

Keywords:
Fusion diagnosis
Neutron coded imaging
Monte Carlo simulation
Image reconstruction
Genetic algorithm
TV algorithm

ABSTRACT

Neutron coded imaging is an effective tool for diagnosing the shape, size and symmetry of deuterium (D)–tritium (T) plasma in inertial confinement fusion (ICF). It can provide an important reference for designing and improving the D–T pellet and confinement configuration. Image reconstruction algorithms play a role of reconstructing the source images from the blurred coded images and the point spread functions (PSFs) of imaging systems. Conventionally, the convolution model is used as the mathematical model for neutron coded imaging reconstruction, but it applies only to the spatially invariant PSF. In this paper, the linear equations model is regarded as the mathematical model for the reconstruction, and it can also be suitable for spatially variant PSF. In the reconstruction, the spatially variant PSFs were simulated through Monte Carlo method. Then an improved genetic algorithm (IGA) for the source image reconstruction was proposed. The comparison of its performance with other types of deterministic algorithms (like the algorithm with total variation (TV) minimization) was conducted, and the results showed that the IGA has better performance in source reconstruction regardless of the utilization of TV sparse prior.

1. Introduction

Nuclear fusion, especially D–T reaction, has been regarded as a powerful method to produce clean energy in recent years. Different from nuclear fission, nuclear fusion produces almost no radioactive waste, but it requires pretty harsh reaction conditions [1]. At present, magnetic confinement fusion (MCF) and inertial confinement fusion (ICF) are the two methods to achieve fusion that lasts for several seconds [2]. Traditional ICF is driven by laser, which employs laser to compress and heat the fuel into plasma state. Another way is termed as "Z-pinch", which utilizes Lorentz force to pinch the metal plasma induced by the current, and further compress and heat the fusion fuel [3]. The information from fusion reaction zone can show the shape, size and symmetry of high density and high temperature plasma, which can further indicate driven symmetry, hydrodynamic instability and radiation ablation in physics. D–T fusion can produce fast neutrons with average energy of 14.1 MeV, which have much stronger penetration ability than X-rays. These neutrons can escape from high density fusion zone. Neutron imaging just makes uses of such information to diagnose the state of fusion zone. In order to get high signal to noise ratio (SNR) and high spatial resolution source image, coded aperture is needed. In neutron coded imaging, coded aperture design and image reconstruction are extremely important. The commonly used coded apertures developed for different applications include: pin hole [4], annular hole [5], penumbra hole [6] and array hole [7].

Image reconstruction algorithms play a role of reconstructing the source images from the blurred coded images and the PSFs of imaging systems. High performance algorithms can achieve high reconstruction accuracy, which can be quantitatively evaluated from some coefficients or criteria (such as, correlation coefficient (CC), normalized root mean square (NRMS) error and normalized mean absolute (NMA) error), with suppressing the system noise. From the view of the based mathematical models and application range, image reconstruction algorithms for coded imaging can be divided into two categories. The first type is based on the convolution model, such as inverse filtering [8], Wiener filtering [9] and Richardson–Lucy (R–L) filtering [10,11], which is only suitable for spatially invariant PSF. The other one is based on the linear equations model, and the reconstruction process can be regarded as solving the linear inverse problems, thus a large number of iteration algorithms developed for solving linear inverse problems can be considered as candidates, which can also be applied to spatially variant reconstruction. Iteration algorithms employ algebraic iteration to minimize the objective function in solving inverse problems, and different algorithms have different minimization objectives and routes. According to the characteristic of different routes, iteration algorithms can be categorized as either deterministic or heuristic. The deterministic

* Corresponding author.
E-mail address: huasi_hu@xjtu.edu.cn (H. Hu).

https://doi.org/10.1016/j.nima.2020.164704
Received 15 April 2020; Received in revised form 28 August 2020; Accepted 22 September 2020
Available online 25 September 2020
0168-9002/

algorithms always reject the new solutions that do not meet the convergence condition (termed as bad solutions) in different iteration steps, such as simultaneous algebraic reconstruction technique (SART) [12] and maximum likelihood expectation maximization (MLEM) [13–16]. The MLEM algorithm is popularly used in coded imaging reconstruction because it considers the feature of the statistical noise and leads to relatively satisfactory results. With the introduction of compressed sensing (CS) theory, sparse prior or regularization has been considered as an important tool to improve the reconstruction accuracy. Many algorithms with sparse constraint has been developed, such as adaptive steepest descent-projection onto convex sets (ASD-POCS) [17], alternating direction total variation minimization (ADTVM) [18] and Chambolle–Pock (CP) [19]. It is worth to mention that those algorithms still belong to the category of deterministic ones. The disadvantage of deterministic algorithms is that they are easily to be trapped in locally optimal solution, which means the accuracy of the reconstructed image still has much space to be raised.

Heuristic algorithms, such as genetic algorithm (GA) and simulated annealing (SA) algorithm, can accept the bad solutions with a certain possibility, which can enhance the ability of algorithms escaping from the locally optimal solution, thus leads to higher reconstruction accuracy theoretically. A few researchers have tried to applied heuristic algorithms to image reconstruction [20–22], however, from the reported results, their performance has not been revealed clearly or not satisfactory enough, because none of the literatures reported a comparable performance with recognized high performance algorithms, like MLEM and the algorithms with TV minimization (they only compared them with filtering algorithms). Therefore, in this paper, the improvements were made based on their work to raise the performance of GA applied in coded imaging reconstruction, and its performance was evaluated by comparing with other types of deterministic algorithms.

2. Method and materials

Z-pinch driven ICF diagnosis is regarded as the research object. We employ the neutron coded imaging system shown in Fig. 1 to diagnose the state of fusion reaction zone. It mainly consists of Z-pinch neutron source, coded aperture and scintillation fiber array. Compared with laser driven ICF, where the size of fusion reaction zone is several hundreds of micrometers, the size in Z-pinch ICF can reach to several millimeters, even centimeter scale. The coded aperture is an inverse radius of curvature (IRC) hole with 6 cm length, which is made of tungsten. The IRC aperture shows better spatially invariant feature than other types of coded apertures, and the design idea is originated from IRC hole in laser driven ICF [23]. The scintillation fiber array has 199 × 199 pixels [24]. Each pixel consists of a fiber core, surrounded cladding and optical cement between the neighborhood pixels from the inside to the outside. The shape of the fiber core is cylinder with a diameter of 500 μm and a length of 5 cm, which is made of BCF-10 (C_8H_8, 1.05 g/cm^3). The thickness of the cladding wall is 25 μm, which is made of acrylic ($C_5H_8O_2$, 1.2 g/cm^3). The material of the optical cement is resin epoxy ($C_{11}H_{12}O_3$, 1.1 g/cm^3). The magnification of the imaging system is 5. The field of view (FOV) is a 1.99 cm × 1.99 cm square.

3. Principle of neutron coded imaging and reconstruction

The mathematical model for neutron coded imaging reconstruction can be expressed as:

$$\boldsymbol{C} = \boldsymbol{PSF} \otimes \boldsymbol{S} + \boldsymbol{N} \tag{1}$$

Where $\boldsymbol{C} = \left(c_{ij}\right) \in \boldsymbol{C}^i \times \boldsymbol{C}^j$ is the coded image; $\boldsymbol{PSF} = \left(psf_{ij}\right) \in \boldsymbol{PSF}^i \times \boldsymbol{PSF}^j$ is the PSF of imaging system; $\boldsymbol{S} = \left(s_{ij}\right) \in \boldsymbol{S}^i \times \boldsymbol{S}^j$ is the source image, i.e. the image to be reconstructed; $\boldsymbol{N} = \left(n_{ij}\right) \in \boldsymbol{N}^i \times \boldsymbol{N}^j$ is the noise; $\otimes$ refers to two-dimensional convolution.

The above model requires the PSF to meet the spatially invariant feature. Only one PSF should be calculated in the reconstruction. However, none of the coded imaging system is strictly spatially invariant even if the IRC coded aperture is used, especially when the FOV is large in Z-pinch ICF diagnosis.

More generally, the mathematical model for neutron coded imaging reconstruction can be described as linear equations:

$$\boldsymbol{C} = \boldsymbol{M}\boldsymbol{S} + \boldsymbol{N} \tag{2}$$

Where $\boldsymbol{C} = \left[c_1, c_2, \ldots, c_i, \ldots, c_u\right]$ is the reshaped coded image; $\boldsymbol{M} = \left(m_{ij}\right) \in \boldsymbol{M}^u \times \boldsymbol{M}^v$ is termed as the transfer matrix, which consists of PSFs within FOV; $\boldsymbol{S} = \left[s_1, s_2, \ldots, s_j, \ldots, s_v\right]$ is the reshaped source image; $\boldsymbol{N} = \left[n_1, n_2, \ldots, n_i, \ldots, n_u\right]$ is the reshaped noise.

The model shown in Eq. (2) transfers the coded imaging reconstruction process into solving the commonly linear inverse problem. The disadvantage of this model is that it requires a large number of PSFs (9801 in our reconstruction), which is a bit time consumption. However, it is suitable for spatially variant reconstruction and does not need the source to be centered in the FOV. PSFs are required to be calculated only one time once the imaging system is determined. Therefore, it deserves to pay some time to calculate PSFs.

4. Spatially variant PSFs simulation

The PSFs and coded image are simulated with the configuration shown in Fig. 1. The materials of each parts are described in Section 2. The simulation is conducted with MCNPX code developed by Los Alamos National Lab, and ENDF/B-VII is used as the cross-section database [25]. The energy deposition of recoiled protons in the fiber is recoded by F6 tally as the detector response. In the PSFs simulation, we first mesh the FOV into 99 × 99 pixels, resulting in the spatial resolution about 100 μm × 100 μm. Then we set a point source at each pixel, which emits neutrons uniformly as D–T fusion neutron spectrum in 4π sr solid angle. In order to reduce the simulation time, 4.77- degree bias sampling angle is employed, which can ensure the neutron beam is blocked by the coded aperture wherever the point source is located at within the FOV. In addition, since the IRC aperture is rotational symmetric, we can only simulate 1/4 PSFs, and the total number of which is 2500 (50 × 50), and 2×10^8 neutrons are emitted in each PSF simulation. As examples of simulated PSFs, Fig. 2(a), (b) and (c) shows the PSFs of point sources located at the position of off-center distance 0 cm, 0.24 cm and 0.49 cm along the horizontal axis respectively; Fig. 2(d) shows the PSF of point source located at off-center distance 0.49 cm along the horizontal axis and 0.49 cm along the vertical axis. The distortion of their shapes can be observed remarkably as the off-center distance increasing, especially in diagonal direction, which is the so-called spatially variant feature. However, the reconstruction based on the convolution model described in Eq. (1) regards the PSF as spatially invariant, i.e. the PSF only moves as the position of the point source changes while keeping the shape unchanged. Therefore, Eq. (1) cannot describe the coded imaging system accurately, which leads to the reconstruction error, and thus we employ the linear equations model for neutron coded imaging reconstruction. It is worth to mention that the speckling in Fig. 2 is caused by the statistical fluctuation of MCNP simulation.

5. Improved genetic algorithm

5.1. Genetic algorithm applied to image reconstruction

Genetic algorithm is a kind of global optimization algorithm, which is constructed based on the law of heredity and evolution of organisms in nature. In the usual optimization design fields, such as process control optimization and radiation shielding design, only several parameters need to be optimized, and simple genetic algorithm (SGA) can be directly applied [26]. However, in image reconstruction field, satisfactory images always consist of several thousands of pixels to be reconstructed, such as CT and coded imaging, and acceptable results are hard to be achieved by directly applying SGA. The reason is that the

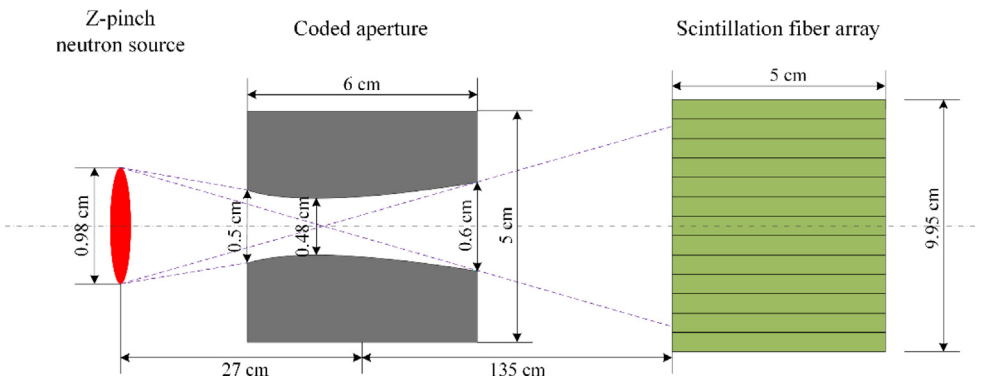

Fig. 1. Neutron coded imaging system for Z-pinch ICF diagnosis.

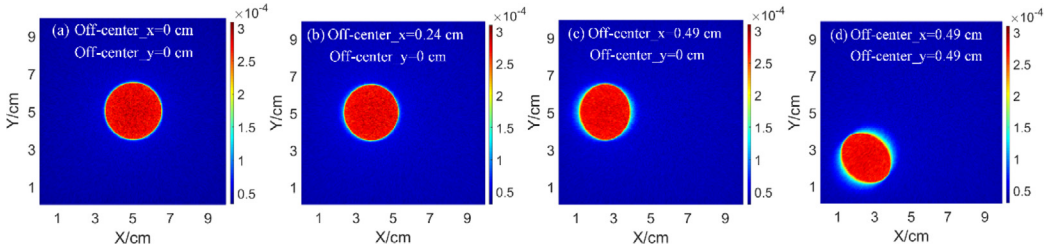

Fig. 2. Spatially variant feature of PSFs in neutron coded imaging (colorbar unit: MeV/g/incident neutron).

algorithm can be easily trapped in locally optimal solution due to the large search space in image reconstruction. Therefore, SGA should be improved in terms of its key links: fitness function, selection, crossover and mutation operators as well as their corresponding factors.

Similar as the objective function in deterministic algorithms, and in consideration of the sparse representation of the image according to compressed sensing theory [27], the fitness function in IGA is described as:

$$f = \|\boldsymbol{C} - \boldsymbol{M}\boldsymbol{S}\|_2^2 + \alpha\Psi(\boldsymbol{S}) \tag{3}$$

Where $\|\boldsymbol{C} - \boldsymbol{M}\boldsymbol{S}\|_2^2$, $\Psi(\boldsymbol{S})$ and α are termed as the fidelity term, the sparse constraint (or regularization) term, and the sparse constraint (or regularization) parameter. The image reconstruction of coded imaging is to minimize the fitness function.

The selection operator in IGA employs the stochastic tournament model combined with simulated annealing and best saving strategies, which has high selection efficiency and is helpful for guaranteeing the diversity of the population and the survival of the individual [21]. The uniform and random row (R)/column (C) crossover operators are combined to raise the efficiency of the crossover of SGA [20], where the crossover is executed between the same or different row or column in different individuals, rather than the same or different pixels. To ensure the continuity feature of the reconstructed object, the neighborhood mutation is usually used [21], where the determination of the pixel value to be reconstructed considers the pixel value of its neighborhoods. Such strategy can guarantee the individual mutating toward the convergence direction. Compared with SGA, the combination of the crossover for the row and column and the neighborhood mutation for the pixel in IGA can ensure the algorithm a higher evolution efficiency. In addition, it deserves to emphasize that the selection, crossover, and mutation are under the control of a group of genetic factors, which classifies IGA as a kind of heuristic algorithm.

5.2. Adaptive crossover and mutation factors

Among the genetic factors, the crossover and mutation factors are the most important ones, which determines the crossover and mutation possibility in GA, and have great impact on the ability of the algorithm in breaking away from the locally optimal solution. Primarily, the crossover factor P_c and mutation factor P_m are fixed numbers in SGA; then M. Srinivas et al. proposed a basic adaptive P_c and P_m to improve the evolution ability of SGA [28], where P_c and P_m can be adaptively adjusted as the fitness value of the individual changes; later, Z. W. Ren et al. suggested another improved adaptive P_c and P_m [29]. Based on their work, our group proposed new ones, and they can show stronger adaptive ability than the previous ones, which are shown as:

$$P_c = \begin{cases} \dfrac{P_{c1}(f_{avg} - f') + P_{c2}(f' - f_{min})}{f_{avg} - f_{min}} & f' < f_{avg} \\ \dfrac{P_{c2}(f_{max} - f') + P_{c3}(f' - f_{avg})}{f_{max} - f_{avg}} & f' \geq f_{avg} \end{cases} \tag{4}$$

$$P_m = \begin{cases} \dfrac{P_{m1}(f_{avg} - f) + P_{m2}(f - f_{min})}{f_{avg} - f_{min}} & f < f_{avg} \\ \dfrac{P_{m2}(f_{max} - f) + P_{m3}(f - f_{avg})}{f_{max} - f_{avg}} & f \geq f_{avg} \end{cases} \tag{5}$$

Where f_{min}, f_{max}, and f_{avg} represent the maximum, minimum and average fitness value of the individuals in the population; f' is the bigger fitness value of the selected two individuals participating in the crossover; f is the fitness value of the individual participating in the mutation, P_{c1}, P_{c2}, P_{c3}, P_{m1}, P_{m2}, P_{m3} are constants, and $P_{c3} < P_{c2} < P_{c1} \in (0, 1)$, $P_{m3} < P_{m2} < P_{m1} \in (0, 1)$.

The new P_c and P_m can change as the relationship of f' and f with f_{min}, f_{max}, and f_{avg} of the population: when f' and f are between f_{min} and f_{avg}, the corresponding P_c and P_m decrease linearly as f' and f increase; when f' and f are between f_{avg} and f_{max}, they also decrease linearly as f' and f increase, but the decreasing rates (slope) are different in the two parts. In consideration of GA is easy to be trapped in locally optimal solution, the improvement of P_c and P_m makes GA more robust, which ensures IGA with them show better performance in image reconstruction.

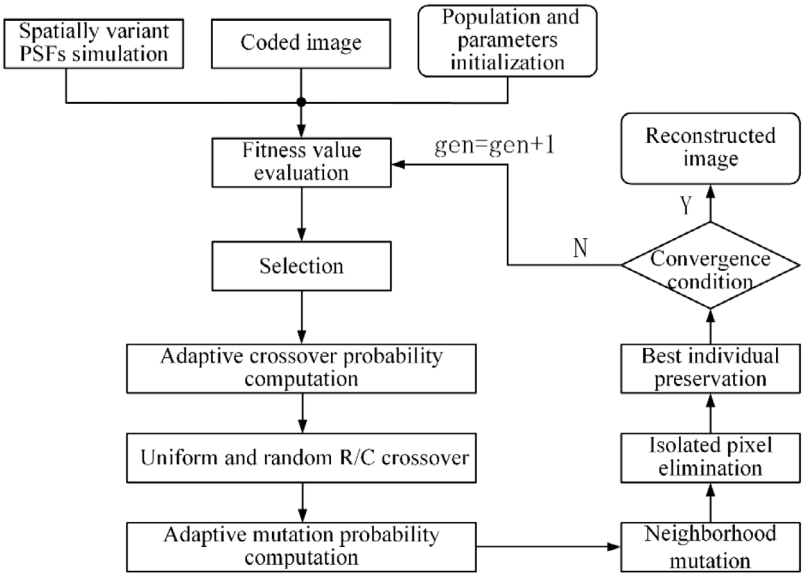

Fig. 3. Flow chart of proposed IGA.

5.3. Isolated pixel treatment

The construction of neighborhood mutation in IGA described in Section 5.1 makes the algorithm search the solution toward the direction of pixel concentration, which can be useful for eliminating the isolated pixels. Here an eliminating possibility factor is proposed to further elevate the ability of the algorithm suppressing the isolated pixel producing:

$$p_e = 1 - \frac{c_e}{\sqrt{\text{gen}}} \tag{6}$$

where c_e is a constant between 0 and 1; gen is the current generation of the population in GA. By means of p_e, the isolated pixel, judged from the pixel value of its neighborhoods, can be eliminated with a certain possibility at every fixed evolution generations, and the possibility decreases as the generation increases until the algorithm meets the convergence condition, which is the number of iterations reaching to the maximum generations or the number of stagnancy iterations reaching to the maximum stagnancy generations (no better results are produced).

Based on the above described main parts of IGA, the executing procedures of IGA are shown in Fig. 3:

(1) Calculating the PSFs of the coded imaging system; Obtaining the coded image from the experiment or simulation; Initializing the population and setting the parameters of the algorithm;
(2) Calculating the fitness values of the individuals;
(3) Evaluating the fitness values and selecting the individuals participating in the following crossover and mutation processes;
(4) Calculating the adaptive crossover possibility with Eq. (4) and the fitness values of the individuals;
(5) Executing the uniform and random R/C crossover for the selected individuals;
(6) Calculating the adaptive mutation possibility with Eq. (5) and the fitness values of the individuals;
(7) Executing the neighborhood mutation for the individuals after the crossover;
(8) Treating the isolated pixels with the possibility described in Eq. (6);
(9) Preserving the best individual;
(10) Looping (2)~(9) until meets the convergence condition, then the reconstructed image is obtained.

6. Reconstructed images

In this section, the performances of IGA is comprehensively investigated: firstly, the effects of the main parts of IGA are revealed; secondly, the comparison of the reconstruction accuracy of IGA with other types of deterministic algorithms are implemented. To quantitatively evaluate the reconstruction accuracy, the Pearson product–moment correlation coefficient c, which describes the similarity of the reconstructed image and the source one, is used:

$$c = \frac{\sum_{i=1}^{v}\left(s_i - \bar{s}_i\right)\left(r_i - \bar{r}_i\right)}{\sqrt{\sum_{i=1}^{v}\left(s_i - \bar{s}_i\right)^2}\sqrt{\sum_{i=1}^{v}\left(r_i - \bar{r}_i\right)^2}} \tag{7}$$

where r_i, s_i, $\bar{r}_i$, $\bar{s}_i$ refer to the pixel value and the average value of all pixels on the reconstructed image and the source image respectively; v represents the number of pixels on them. $c \in (0, 1)$, and larger c means the similarity between the reconstructed image and the source one is higher.

The feature of heuristic algorithm is its random minimization route, therefore, the reconstructed results are different for reconstructions at different time. Fig. 4(a) and (b) show the source image ("E" letter with 7.15 mm × 7.15 mm size) and coded image under 10^{12} neutron yield. Fig. 4(c) and (d) show the reconstructed images by IGA through 1 reconstruction and average of multiple reconstructions respectively. The pixel value on the source image and reconstructed images has been normalized by the maximum pixel value of the whole image. It can be observed that the high accuracy image can be achieved through average of 10 reconstructions. Compared with 1 reconstruction, average of 10 reconstructions can enhance the capability of the algorithm in restoring the edge of reconstruction objects, and further improve the whole reconstruction accuracy. Therefore, the reconstructed images by IGA are the results through average of 10 reconstructions in the following sections.

6.1. Effect of main parts of IGA

In the proposed IGA, the sparse constraint, the new adaptive crossover and mutation factors and isolated pixel treatment are the main parts ensuring the high performance of the algorithm. In order to show the effect of each parts, we reconstructed the"E" letter by IGA with one part removed per time respectively (Fig. 5). The results show the above three parts have significant impact on the reconstructed results; the remarkable results can be achieved by combining those parts. In other words, without the improvements of the algorithm, remarkable results cannot be achieved.

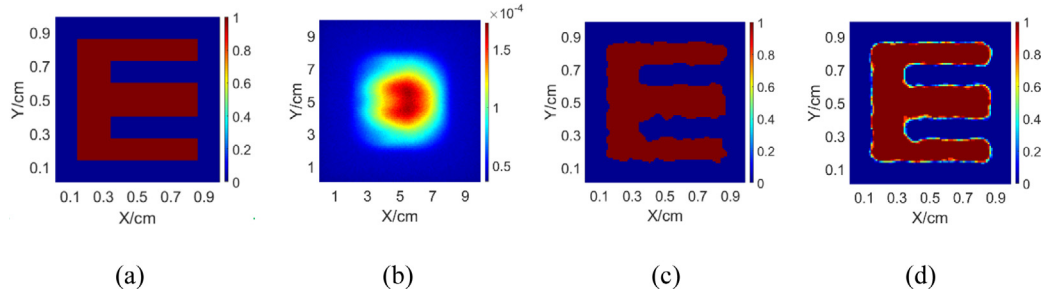

Fig. 4. Random feature of IGA: (a) source image; (b) coded image (colorbar unit: MeV/g/incident neutron); (c) 1 reconstruction, $c = 0.9273$; (d) average of 10 reconstructions, $c = 0.9563$.

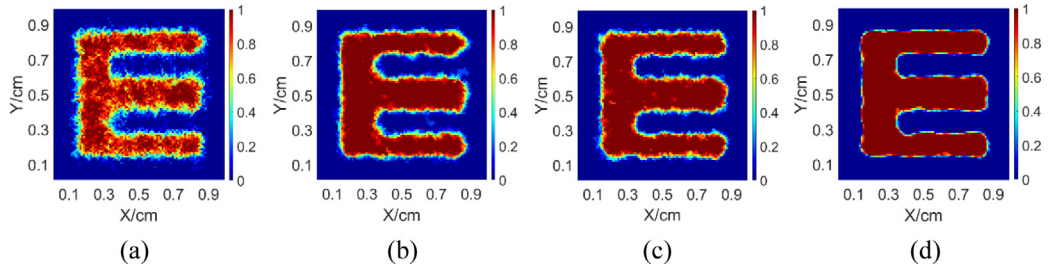

Fig. 5. Effect of the main parts of IGA: (a) without sparse constraint, $c = 0.9138$; (b) without adaptive crossover and mutation factors, $c = 0.9382$; (c) without isolated pixel treatment, $c = 0.9417$; (d) combination of all parts, $c = 0.9563$.

6.2. Introduction to deterministic algorithms

SART algorithm is a typical algorithm to solve linear inverse problem, which has been proved to converge to a weighted least square solution of the linear equations [30]. Based on the SART algorithm, SART with TV minimization algorithm was developed. In order to keep the comparison of the reconstruction accuracy of different algorithms under a fair environment, it is better to select the algorithms which share the same sparse constraint terms and only keep the minimization solving methods different. Based on this principle, we have selected SART to compare with IGA without sparse constraint term and SART with TV to compare with IGA with TV constraint. The iteration formula of SART is:

$$s_j^{(k+1)} = s_j^{(k)} + \lambda \frac{\sum_{i=1}^{u} \left[m_{ij} \frac{c_i - \sum_{j=1}^{v} m_{ij} s_j}{\sum_{j=1}^{v} m_{ij}} \right]}{\sum_{i=1}^{u} m_{ij}} \tag{8}$$

Where s_j, c_j and m_{ij} are the element in the reshaped source image vector, the reshaped coded image vector and the transfer matrix described in Section 3, $j = 1, 2, \ldots, v$; k is the number of iterations; λ is the relaxing factor. TV minimization is a famous sparse representation in the image process and reconstruction fields. It considers the image is sparse in gradient domain, which can be described as:

$$\|S\|_{TV} = \sum_{p,q} \sqrt{\left(s_{p,q} - s_{p-1,q}\right)^2 + \left(s_{p,q} - s_{p,q-1}\right)^2} \tag{9}$$

Where $s_{p,q}$ is the element in the source image matrix; $s_{p-1,q}$ and $s_{p,q-1}$ are its neighborhoods in vertical and horizontal directions respectively. SART with TV algorithm employs SART algorithm to minimize the fidelity term and steepest descent method to minimize TV sparse constraint term in Eq. (3), which has been proved to be a reliable and robust algorithm in the image reconstruction field.

In addition, the selection of convergence condition and algorithm parameters are important in algorithm comparison. In this paper, the convergence condition of the above two algorithms is $\left\|\boldsymbol{C} - \boldsymbol{M}\hat{\boldsymbol{S}}\right\|_2^2 / \|\boldsymbol{S}\|_2^2 \le \eta$, where η are 9×10^{-4} and 2.5×10^{-4} for SART and SART+TV algorithms; the optimal parameter is selected based on achieving maximum c in formula (7), and $\lambda = 5{\times}10^{-17}$. The selected parameters for the proposed IGA are: population size = 50, $P_{c1} = 0.9$, $P_{c2} = 0.5$, $P_{c3} = 0.1$, $P_{m1} = 0.1$, $P_{m2} = 0.05$, $P_{m3} = 0.005$, $c_e = 0.5$, maximum generations = 10000, maximum stagnancy generations = 1000, and α varies for different coded images based on achieving maximum c. Those parameters are selected by plenty of attempts, and they are recommended for IGA.

6.3. Comparison of IGA with SART and IGA with TV with SART with TV

Here we compare the performance of IGA with selected deterministic algorithms (shown in Fig. 6). It can be observed that the reconstruction accuracy of IGA without and with TV sparse constrain term is much higher than that of SART and SART with TV: c increases from 0.8218 to 0.9138 for SART to IGA without TV; c increases from 0.9266 to 0.9563 for SART with TV to IGA with TV. Specifically, the size of "E" letter is changed a little on the image reconstructed by SART, such as, the width of the middle "transverse line" of "E" letter is changed from 0.195 cm to 0.125 cm at X = 0.396 cm. It seems like the algorithm is excessively iterated. But the reduction of number of iterations will cause a large number of streak artifacts appear, which further lowers c. The shape of "E" letter is deformed a bit, such as, the changing extent of the middle "transverse line" of "E" letter at X = 0.396 cm, 0.515 cm and 0.762 cm is 0.07 cm, 0.075 cm and 0.04 cm respectively. The reason is that the noise can be amplified as the iteration proceeding due to the ill-posed feature of Eq. (2). However, only some dot artifacts appear on the edge of the image reconstructed by IGA, and the size and shape of"E" letter can be basically restored. Therefore, IGA shows stronger noise suppression ability than SART without TV constraint. With TV constraint term added into IGA and SART, the results have been improved significantly: c increases from 0.8218 to 0.9266 for SART to SART with TV; c increases from 0.9138 to 0.9563 for IGA without TV to IGA with TV. For the SART with TV, the streak artifacts have been suppressed by the TV constraint successfully. The shape restoration ability can be enhanced by balancing SART fidelity and TV constraint terms. However, the piecewise artifacts appear on the image. For the IGA with TV, the dot artifacts have also been suppressed by the TV constraint. In general, the reconstruction accuracy of IGA with TV is much higher than that of SART with TV. The reason is the random minimization route which ensures the algorithm with high possibility to escape from the locally optimal solution.

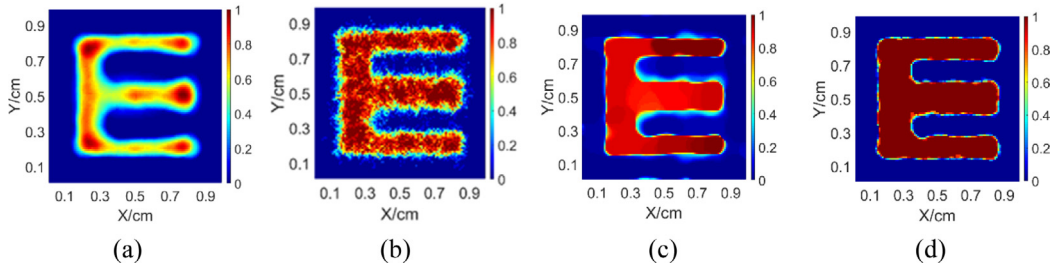

Fig. 6. Comparison of images reconstructed by deterministic and heuristic algorithms: (a) SART, $c = 0.8218$; (b) IGA without TV, $c = 0.9138$; (c) SART with TV, $c = 0.9266$; (d) IGA with TV, $c = 0.9563$.

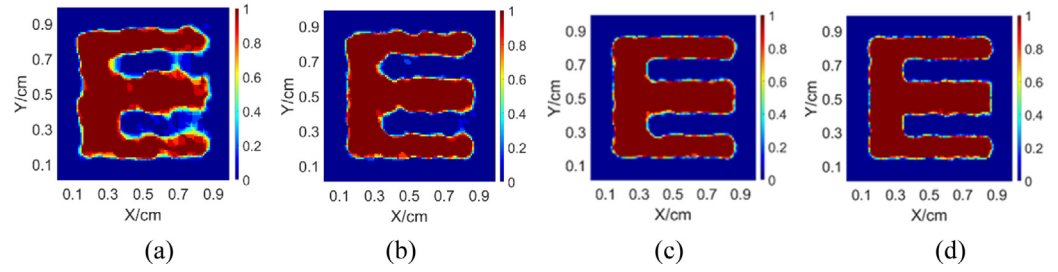

Fig. 7. Reconstruction under low neutron yields: (a) yield = 10^{10}, $c = 0.9130$; (b) yield=10^{11}, $c = 0.9395$; (c) yield = 10^{12}, $c = 0.9563$; (d) yield = 10^{13}, $c = 0.9600$.

6.4. Reconstruction under different neutron yields

For Z-pinch driven ICF diagnosis, the neutron yields of different facilities can range from 10^{10}~10^{13}, or even lower, which is much lower than that of laser driven ICF facilities, like the National Ignition Facility (NIF) [31] with a neutron yield reaching up to 10^{17}. Low neutron yields mean the high noise level, which requires strong noise suppression ability of the algorithm. Therefore, we also have checked the reconstruction performance of IGA under low neutron yields (Fig. 7). Both of the PSFs and coded images for reconstruction were obtained from MCNP simulations. The results demonstrate that IGA is robust and exhibits good performance in low neutron yields reconstruction.

7. Discussion and conclusion

A heuristic algorithm for neutron coded imaging reconstruction based on simple genetic algorithm has been proposed. The corresponding performance when applied to spatially variant PSFs (obtained from Monte Carlo simulation) reconstruction was checked. The reconstructed results show higher reconstruction accuracy of the algorithm than that of SART algorithm without and with TV constraint. The fundamental reason is the heuristic algorithm always accepts the bad solutions with a certain possibility. Thus the algorithm can escape from the locally optimal solution with higher possibility when compared with deterministic algorithms, and further shows stronger noise suppression ability. The proposed algorithm also shows good performance in low neutron yields reconstruction. TV has been used as the sparse representation in IGA, the performance of IGA with other sparse representations, such as cosine transformation and wavelet transformation, will be investigated in the future. It is worth to mention that the Z-pinch source is treated as a 2-dimensional (D) source in this paper. The 3D image can be reconstructed with simulated PSFs for the point sources on each slice along the axis of imaging system, and the proposed algorithm is also suitable for 3D reconstruction. Although the algorithm is proposed based on the spatially variant PSF reconstruction, it can also be applied to spatially invariant PSF reconstruction in neutron coded imaging. Furthermore, it can be extended to radioactive source localization.

CRediT authorship contribution statement

Mingfei Yan: Conceptualization, Methodology, Software, Writing - original draft. **Huasi Hu:** Supervision. **Guang Hu:** Investigation, Formal analysis. **Zhihua Liu:** Validation, Writing - review & editing. **Chao He:** Data curation. **Qiang Yi:** Visualization.

Declaration of competing interest

The authors declare that they have no known competing financial interests or personal relationships that could have appeared to influence the work reported in this paper.

Acknowledgments

This research is supported by the NSAF Joint Fund of China (Grant No. U1830128) and the National Natural Science Foundation of China (Grant Nos. 11975182 and 11875214)

References

[1] D.J. Rose, Controlled nuclear fusion: status and outlook, Science 172 (1971) 797–808.
[2] R. Betti, P.Y. Chang, B.K. Spears, K.S. Anderson, J. Edwards, M. Fatenejad, J.D. Lindl, R.L. McCrory, R. Nora, D. Shvarts, Thermonuclear ignition in inertial confinement fusion and comparison with magnetic confinement, Phys. Plasmas 17 (2010) 058102.
[3] M.G. Haines, A review of the dense Z-pinch, Plasma Phys. Control. Fusion 53 (2011) 093001.
[4] M. Gieles, H.W.A.M. de Jong, F.J. Beekman, Monte Carlo simulations of pinhole imaging accelerated by kernel-based forced detection, Phys. Med. Biol. 47 (2002) 1853–1867.
[5] L. Disdier, A. Rouyer, I. Lantuéjoul, O. Landoas, J.L. Bourgade, Inertial confinement fusion neutron images, Phys. Plasmas 13 (2006) 056317.
[6] K.A. Nugent, B. Luther-Davies, Application of penumbral imaging to thermonuclear neutrons, J. Appl. Phys. 58 (1985) 2508.
[7] T. Ueda, S. Fujioka, S. Nozaki, R. Azuma, Y.W. Chen, H. Nishimura, A uniformly redundant imaging array of penumbral apertures coupled with a heuristic reconstruction for hard X-ray and neutron imaging, Rev. Sci. Instrum. 81 (2010) 073505.
[8] H. Matsuo, A. Iwata, I. Horiba, N. Suzumura, Three-dimensional image reconstruction by digital tomo-synthesis using inverse filtering, IEEE Trans. Med. Imaging 12 (1993) 307–313.
[9] W.K. Pratt, Generalized wiener filtering computation techniques, IEEE Trans. Comput. c-21 (1972) 636–641.

[10] W.H. Richardson, Bayesian-based iterative method of image restoration, J. Opt. Soc. Amer. 62 (1972) 55–59.
[11] L.B. Lucy, An iterative technique for the rectification of observed distribution, Astron. J. 79 (1974) 745–754.
[12] A.H. Andersen, A.C. Kak, Simultaneous algebraic reconstruction technique (SART): a superior implementation of the ART algorithm, Ultrason. Imaging 6 (1984) 81–94.
[13] L.A. Shepp, Y. Vardi, Maximum likelihood reconstruction for emission tomography, IEEE Trans. Med. Imaging mi-1 (1982) 113–122.
[14] K. Lange, R. Carson, EM reconstruction algorithms for emission and transmission tomography, J. Comput. Assist. Tomogr. 8 (1984) 306–316.
[15] Z.Q. Zhao, Y.D. Hao, Y.T. Yuan, W. Jiang, W.Y. Miao, Y.K. Ding, Nucl. Instrum. Methods Phys. Res. A 613 (2010) 141–144.
[16] P. Volegov, C.R. Danly, D.N. Fittinghoff, G.P. Grim, N. Guler, N. Izumi, T. Ma, F.E. Merrill, A.L. Warrick, C.H. Wilde, D.C. Wilson, Neutron source reconstruction from pinhole imaging at national ignition facility, Rev. Sci. Instrum. 85 (2014) 023508.
[17] E.Y. Sidky, X.C. Pan, Image reconstruction in circular cone-beam computed tomography by constrained, total-variation minimization, Phys. Med. Biol. 53 (2008) 4777–4807.
[18] L.Y. Wang, A.L. Cai, H.M. Zhang, B. Yan, L. Li, G.E. Hu, S.L. Bao, Distributed CT image reconstruction algorithm based on the alternating direction method, J. X-ray Sci. Technol. 23 (2015) 83–99.
[19] A. Chambolle, T. Pock, A first-order primal–dual algorithm for convex problems with applications to imaging, J. Math. Imaging Vision 40 (2011) 120–145.
[20] Y.W. Chen, Z. Nakao, K. Arakaki, Genetic algorithms applied to neutron penumbral imaging, Opt. L. 4 (1997) 209–215.
[21] T.K. Zhang, H.S. Hu, Q.G. Jia, F.N. Zhang, D. Chen, Z.H. Li, Y.L. Wu, Z.H. Liu, G. Hu, W. Guo, Genetic algorithms applied to reconstructing coded imaging of neutrons and analysis of residual watermark, Rev. Sci. Instrum. 83 (2012) 113505.
[22] S. Nozaki, Y.W. Chen, Heuristic reconstructions of neutron penumbral images, Rev. Sci. Instrum. 75 (2004) 3980.
[23] R.A. Lerche, D. Ress, R.J. Ellis, S.M. Lane, Neutron penumbral imaging of laser-fusion targets, Laser Part. Beams 9 (1991) 99–118.
[24] Q.G. Jia, H.S. Hu, F.N. Zhang, T.K. Zhang, W. Lv, Y.P. Zhan, Z.H. Liu, Simulation study of using high-Z EMA to suppress recoil protons crosstalk in scintillating fiber array for 14.1 MeV neutron imaging, IEEE Trans. Nucl. Sci. 60 (2013) 4727–4736.
[25] D.B. Pelowitz (Ed.), MCNPX Users Manual Version 2.7.0, LA-CP-11-00438, 2011.
[26] D. Whitley, A genetic algorithm tutorial, Stat. Comput. 4 (1994) 65–85.
[27] D.L. Donoho, Compressed sensing, IEEE Trans. Inform. Theory 52 (2006) 1289–1306.
[28] M. Srinivas, L.M. Patnaik, Adaptive probabilities of crossover and mutation in genetic algorithms, IEEE Trans. Syst. Man Cybern. 24 (1994) 656–667.
[29] J. Zhang, Y.S. Zhang, Z.H. Wang, J.X. Duan, X.X. Huang, An efficient optimization algorithm for extreme value of nonlinear function based on the SAGA and BP algorithm, IEEE Access 7 (2019) 133058–133068.
[30] M. Jiang, G. Wang, Convergence of the Simultaneous Algebraic Reconstruction Technique (SART), IEEE Trans. Image Process. 12 (2003) 957–961.
[31] P.L. Volegov, C.R. Danly, D.N. Fittinghoff, N. Guler, F.E. Merrill, C.H. Wilde, Self characterization of a coded aperture array for neutron source imaging, Rev. Sci. Instrum. 85 (2014) 123506.